UV–Ozone Interfacial Modification in Organic Transistors for High-Sensitivity NO₂ Detection

Wei Huang, Xinming Zhuang, Ferdinand S. Melkonyan, Binghao Wang, Li Zeng, Gang Wang, Shijiao Han, Michael J. Bedzyk, Junsheng Yu,* Tobin J. Marks,* and Antonio Facchetti*

A new type of nitrogen dioxide (NO₂) gas sensor based on copper phthalo-cyanine (CuPc) thin film transistors (TFTs) with a simple, low-cost UV–ozone (UVO)-treated polymeric gate dielectric is reported here. The NO₂ sensitivity of these TFTs with the dielectric surface UVO treatment is ≈400× greater for [NO₂] = 30 ppm than for those without UVO treatment. Importantly, the sensitivity is ≈50× greater for [NO₂] = 1 ppm with the UVO-treated TFTs, and a limit of detection of ≈400 ppb is achieved with this sensing platform. The morphology, microstructure, and chemical composition of the gate dielectric and CuPc films are analyzed by atomic force microscopy, grazing incident X-ray diffraction, X-ray photoelectron spectroscopy, and Fourier transform infrared spectroscopy, revealing that the enhanced sensing performance originates from UVO-derived hydroxylated species on the dielectric surface and not from chemical reactions between NO₂ and the dielectric/semiconductor components. This work demonstrates that dielectric/semiconductor interface engineering is essential for readily manufacturable high-performance TFT-based gas sensors.

Economic growth and quality-of-life improvement during the past decades have dramatically increased worldwide energy consumption. Most of the energy needs for transportation, domestic, and industrial usage originate from combustion of fossil fuels, which are not renewable and release toxic gases into the atmosphere.[1] Especially in developing countries, massive production of harmful gases has become problematic to society.[2] Therefore, accurate, cost-effective means of monitoring and detecting air quality is of paramount importance since these gases do not only pose environmental concerns but also endanger public health.[3]

Among the harmful environmental gases, nitrogen dioxide (NO₂) is particularly dangerous.[4] Although short-term exposure (1–3 h) of healthy individuals to NO₂ at concentrations <1 ppm does not typically induce adverse pulmonary effects, long-term exposure to low NO₂ concentrations (≈1 ppm) can impair respiratory function and increase the risk of emphysema and bronchitis.[5] Individuals with asthma or allergies experience negative pulmonary function at NO₂ concentration as low as 0.2–0.6 ppm.[6] Moreover, ≥10 ppm NO₂ concentration causes immediate distress, including edema, nose and throat irritation, and >100 ppm can cause death by asphyxiation.[7] Furthermore, NO₂ is a component of acid rain and accelerates the formation of microscopic particles in the air.

Currently several technologies, including chemiluminescent, electrochemical, resistive, and optical sensing are used for NO₂ detection.[8] Although some commercial sensors have low limits of detection (LOD), usually below ppm, even ppt level, and good selectively, they usually are limited by high cost and/or high operating power consumption. In contrast, simple, readily manufactured sensors based on organic thin-film transistors (OTFTs) potentially offer low-cost, low power consumption, and high performance, and are regarded as promising candidates for next-generation gas sensors.[9–12] Moreover, OTFT-based gas sensors can be integrated with standard integrated circuit (IC) technologies, making it possible to fabricate smart, portable electronic noses integrable with cell-phones, laptops, and smart appliances.[13]

To enhance OTFT sensor performance, typical approaches have focused on the organic semiconductor (OSCs) and gate dielectric materials.[14–17] Thus, Huang used naphthalene-tetra-carboxylic diimide derivatives and copper phthalocyanine (CuPc) to fabricate OTFT sensor arrays, showing the potential for rapid and selective volatile analyte detection.[18] Sensitive dielectric and interface design was also adopted for realizing high-performance TFT-based gas, light, and biosensors.[19–21] Shaymurat

Dr. W. Huang, X. Zhuang, S. Han, Prof. J. Yu
State Key Laboratory of Electronic Thin Films and Integrated Devices
School of Optoelectronic Information
University of Electronic Science and Technology of China (UESTC)
Chengdu 610054, China
E-mail: jsyu@uestc.edu.cn
Dr. W. Huang, Prof. F. S. Melkonyan, Dr. B. Wang, Dr. G. Wang,
Prof. T. J. Marks, Prof. A. Facchetti
Department of Chemistry
Northwestern University
2145 Sheridan Road, Evanston, IL 60208, USA
E-mail: t-marks@northwestern.edu; a-facchetti@northwestern.edu
L. Zeng, Prof. M. J. Bedzyk
Department of Materials Science and Engineering and Applied Physics
Program
Northwestern University
2220 Campus Drive, Evanston, IL 60208, USA
Prof. A. Facchetti
Flexterra Inc.
8025 Lamon Avenue, Skokie, IL 60077, USA

The ORCID identification number(s) for the author(s) of this article can be found under https://doi.org/10.1002/adma.201701706.

DOI: 10.1002/adma.201701706

developed high-performance SO_2 sensors with a 0.5 ppm LOD using an air gap as the dielectric layer.[22] Another strategy focuses on creating highly sensitive organic semiconductors via chemical modifications which combine charge-carrying cores with peripheral analyte receptors. Implementing semiconductors with functional groups that strongly bind the target analyte can enhance both sensitivity and selectivity.[23–27] Thus, Katz increased OTFT ammonia response using strongly Lewis acidic tris(pentafluorophenyl)borane as the receptor, affording an LOD of 350 ppb.[24] Utilizing optimized device geometries is also effective in enhancing TFT gas sensor performance. Thus, ultrathin and/or structured OSCs can enlarge the surface-to-volume ratio, thereby enhancing sensitivity and lowering the response time.[28–32] Mirza reported NO_2 gas sensing with vapor-deposited ultrathin/sub-monolayer pentacene films which exhibited high sensitivity, fast response/recovery time, an LOD of 100 ppb, and excellent reproducibility.[33] Top-gate OTFTs with sensitive gate dielectrics were also reported by Klug to detect low-concentrations of NH_3.[34] From these results it can be surmised that high-sensitivity OTFT gas sensors can require highly sensitive OSCs and unconventional TFT structures, which may introduce complexity and increase fabrication cost. Thus, achieving high-performance devices while preserving straightforward, low-cost fabrication would be highly desirable.[35]

Here we realize ultrasensitive OTFT-based NO_2 sensors by implementing a simple, low-cost UV–ozone (UVO) treatment of the gate dielectric. We show that the dielectric surface chemistry, and thus the interfacial trap density, can be controlled by simply adjusting the UVO treatment time (t_{UVO}). These trap sites influence the OTFT performance for both unexposed and NO_2 vapor exposed devices. Upon NO_2 exposure, the analyte molecules strongly adsorb to the UVO-induced functional groups, which is essential for achieving ultrasensitive devices. The sensitivities at $[NO_2] = 1$ and 30 ppm are enhanced by ≈50 and ≈400 times, respectively, upon t_{UVO} optimization. Furthermore, the enhanced NO_2 adsorption on the UVO-treated dielectric surface enables these devices to retain NO_2 at room temperature in ambient, essential for cost-effective NO_2 sensor integration.

The present TFT configuration and device fabrication process are shown in **Figure 1**a. Glass with patterned ITO substrates as gate electrodes were cleaned by sonication in acetone, deionized (DI) water, and isopropyl alcohol for 15 min, followed by O_2 plasma treatment for 5 min (20 W). Poly(vinyl alcohol) (PVA, M_w ≈ 146 000–186 000; 40 mg mL^{-1} in high purity water) was spin-coated onto the ITO substrates and annealed at 70 °C for 1 h. Polystyrene (PS, M_w ≈ 280 000; 30 mg mL^{-1} in o-xylene) was then spin-coated on top and baked at 120 °C for 1.0 h to remove residual solvents. A double-layer dielectric is used here to provide good adhesion to the gate electrode and achieve excellent insulating properties. Prior to deposition of the organic semiconductor, the dielectric film was exposed to UV light at 185 and 253.7 nm (UVO-Cleaner 42, Jelight
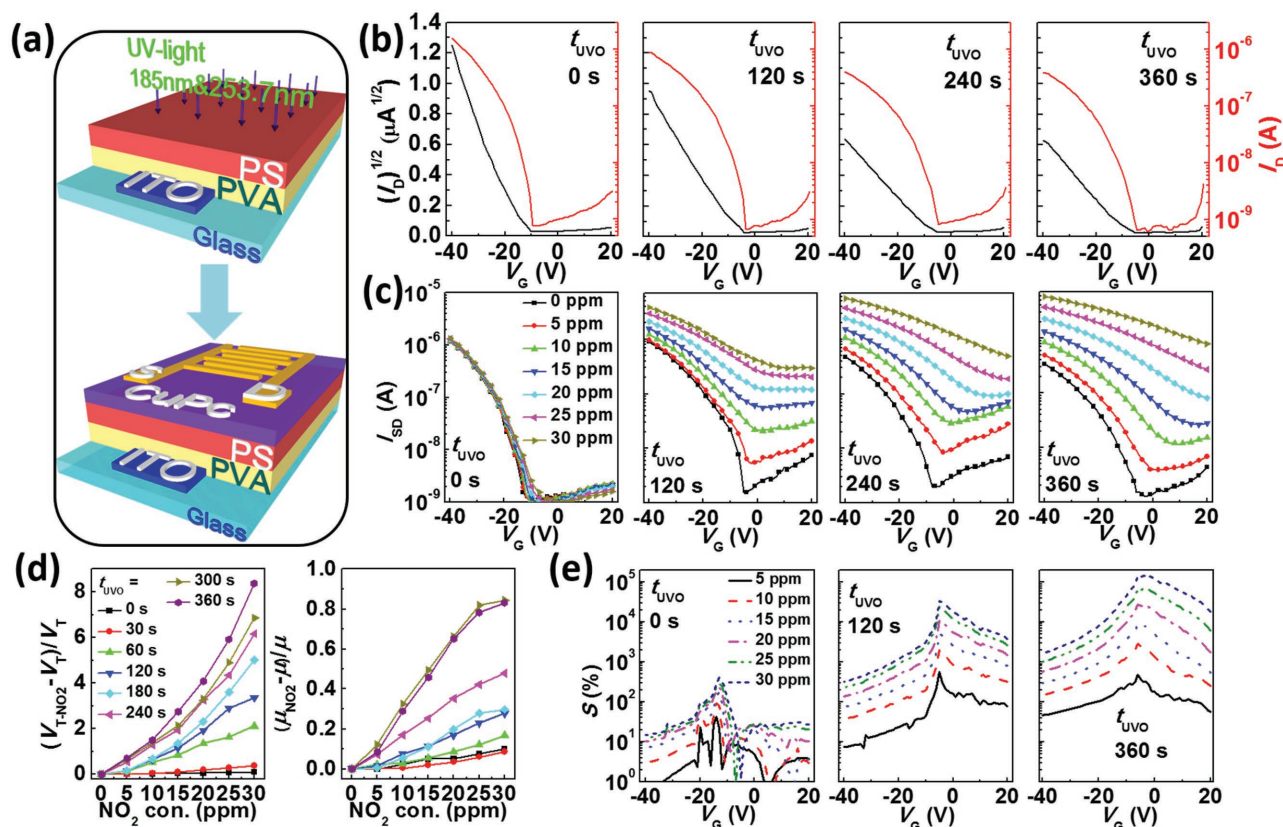

Figure 1. a) Bottom gate CuPc OTFT structure and UVO treatment of the gate dielectric surface. b) Transfer curves for different t_{UVO} values. c) Transfer curves for the indicated t_{UVO} values and different NO_2 concentrations. d) Percentage V_T and mobility variations as a function of t_{UVO} and NO_2 concentrations. e) Sensitivity (S)–V_G plots for the indicated t_{UVO} values and NO_2 concentrations.

**ADVANCED
SCIENCE NEWS**

www.advancedsciencenews.com

**ADVANCED
MATERIALS**

www.advmat.de

Table 1. Summary of the CuPc TFT sensor performance parameters for different t_{UVO} of the gate dielectric.

t_{UVO} [s]	0	30	60	120	180	240	300	360
I_{ON} [10^{-6} A]	1.6 ± 0.3	1.9 ± 0.5	1.2 ± 0.2	0.92 ± 0.15	0.52 ± 0.09	0.41 ± 0.11	0.32 ± 0.07	0.29 ± 0.09
V_{ON} [V]	-10.5 ± 2.1	-7.2 ± 1.8	-4.7 ± 2.5	-4.2 ± 4.1	-4.5 ± 3.6	-5.1 ± 2.3	-5.0 ± 1.9	-4.7 ± 2.6
μ [10^{-3} cm^2 V^{-1} s^{-1}]	3.1 ± 0.4	3.2 ± 0.5	1.6 ± 0.2	1.3 ± 0.3	0.79 ± 0.08	0.56 ± 0.4	0.49 ± 0.06	0.51 ± 0.04
V_T [V]	-14.2 ± 2.1	-12.3 ± 1.5	-9.1 ± 2.3	-7.1 ± 3.1	-7.1 ± 2.1	-6.8 ± 1.5	-6.8 ± 2.0	-7.0 ± 2.1

Company Inc.) for a time (t_{UVO}) varying from 0 to 360 s. Next, a 10 nm CuPc film was deposited by thermal evaporation. The transistors were then completed by depositing 40 nm thick gold source and drain electrodes via thermal evaporation using a metal shadow mask to form a channel length of 100 µm and width of 1.0 cm. Before establishing the response of the platform to NO$_2$, the effect of t_{UVO} on the CuPc TFT performance was investigated, and data are summarized in **Table 1**.

Figure 1b and Figure S1 (Supporting Information) indicate that the I–V transfer characteristics are strongly affected by t_{UVO}. Thus, the on-current (I_{ON}, drain current measured at $V_D = V_G = -40$ V) of the untreated device ($\approx 1.6 \times 10^{-6}$ A) first slightly increases to $\approx 1.9 \times 10^{-6}$ A for $t_{UVO} = 30$ s, next decreases to $\approx 1.2 \times 10^{-6}$ and $\approx 3.2 \times 10^{-7}$ A as t_{UVO} is increased from 60 to 300 s, respectively, and finally stabilizes at $\approx 3.2 \times 10^{-7}$ A for $t_{UVO} > 300$ s. Meanwhile, a shift of the turn-on voltage (V_{ON}, the gate voltage at which the current start increasing sharply) toward positive values is observed [V_{ON} (t_{UVO}) = -10.5 V (0 s); -7.2 V (30 s); -4.7 V (60 s)]. When t_{UVO} exceeds 60 s, V_{ON} stabilizes at ≈ -4.5 V. Moreover, as t_{UVO} increases from 30 to 300 s, the on/off current ratio monotonically falls from $\approx 2 \times 10^3$ ($t_{UVO} = 30$ s) to $\approx 4 \times 10^2$ ($t_{UVO} = 300$ s). To verify that the TFT performance variations are not due to major changes in the gate insulator dielectric properties, the leakage current and capacitance of the PVA/PS gate dielectric for different UVO exposure times were measured in MIM capacitors of the structure, ITO/dielectric/Au (Figure S2, Supporting Information). The leakage current and capacitance values of all samples exhibit small variations with t_{UVO}, with the current density remaining $< \approx 10^{-7}$ A cm^{-2} (at ± 20 V) and the capacitance slightly increasing from 10.2 nF cm^{-2} ($t_{UVO} = 0$ s) to 11.9 nF cm^{-2} ($t_{UVO} = 360$ s). This reflects the mild etching effects of UVO treatment on polymer films,[36] with the present dielectric layer thickness contracting by ≈ 20 nm (from 530 to 510 nm) for $t_{UVO} = 360$ s.

From the I–V characteristics, the FET performance parameters were extracted using standard MOSFET equations,[3,13] and mobility (μ) and threshold voltage (V_T) data are summarized in Table 1. The TFT data indicate that OTFT performance of these devices stabilize when $t_{UVO} > 300$ s. Thus, μ decreases from 3.1×10^{-3} cm^2 V^{-1} s^{-1} ($t_{UVO} = 0$ s) to 1.3×10^{-3} cm^2 V^{-1} s^{-1} ($t_{UVO} = 120$ s) to 4.9×10^{-4} cm^2 V^{-1} s^{-1} ($t_{UVO} = 300$ s). In parallel, a consistent positive shift of V_T is observed [V_T (t_{UVO}) = -14.2 V (0 s); -9.1 V (60 s); -7.1 V (120 s)], and stabilizes at ≈ -7.0 V ($t_{UVO} \geq 120$ s). Variations of the electrical parameters with t_{UVO} in our OTFTs are in line with previous reports of pentacene TFTs with UVO-treated polymeric dielectrics.[37–39]

The sensor performance of the present CuPc TFTs with/without UVO-treated dielectric surfaces was characterized using gaseous NO$_2$ as the analyte in the 5–30 ppm concentration range. The details of the I–V parameters are summarized in Table S1 (Supporting Information). In a typical experiment, the OTFT sensor was placed in an airtight test chamber (≈ 2.4 mL), and a mixture of dry air and 50 ppm NO$_2$ gas mixed in appropriate concentrations was introduced into the test chamber by mass flow controllers (see Figure S3, Supporting Information). The flow rate in the experiment was fixed at 100 sccm (standard cm^3 min^{-1}), and OTFT I–V measurements were carried out after 2 min of NO$_2$ exposure in the test chamber. Figure 1c and Figure S4 (Supporting Information) show that the NO$_2$ sensitivity of this platform strongly depends on UVO processing and t_{UVO}. The I–V characteristics clearly demonstrate that after the dielectric surface is exposed to UVO, the NO$_2$ sensitivity of the I–V characteristics increase dramatically. Thus, for TFTs with a pristine PS/PVA dielectric, as the [NO$_2$] increases, there is only a slightly increase of the I_{ON} [from 1.19×10^{-6} A ([NO$_2$] = 0 ppm) to 1.27×10^{-6} A ([NO$_2$] = 15 ppm) to 1.36×10^{-6} A ([NO$_2$] = 30 ppm)] and a small shift of V_{ON} [from -12 V (0 ppm NO$_2$) to -9 V (15 ppm NO$_2$) to -8 V (30 ppm NO$_2$)]. No obvious off-current (I_{OFF}) variations were observed, which remains at $\approx 10^{-9}$ A. In marked contrast, for the UVO-treated devices, the transfer curves exhibit considerable variations upon gas exposure. For the device with w I_{ON} increases from 1.14×10^{-6} A ([NO$_2$] = 0 ppm) to 1.77×10^{-6} A ([NO$_2$] = 15 ppm) to 3.18×10^{-6} A ([NO$_2$] = 30 ppm), V_{ON} shifts from -4 V ([NO$_2$] = 0 ppm) to 1 V ([NO$_2$] = 15 ppm) to 8 V ([NO$_2$] = 30 ppm), and I_{OFF} increases from 1.47×10^{-9} A ([NO$_2$] = 0 ppm) to 1.3×10^{-8} A ([NO$_2$] = 15 ppm) to 6.06×10^{-8} A ([NO$_2$] = 30 ppm). Furthermore, when exposed to NO$_2$, the variations of the transfer curves enlarge as t_{UVO} increases up to ≥ 300 s, at which time they stabilize. Thus, as shown in Figure 1c and Figure S4 (Supporting Information), for $t_{UVO} = 300$ s, I_{ON} increases from 2.89×10^{-7} A ([NO$_2$] = 0 ppm) to 1.11×10^{-6} A ([NO$_2$] = 15 ppm) to 4.75×10^{-6} A ([NO$_2$] = 30 ppm) while V_{ON} shifts considerably from -5 V ([NO$_2$] = 0 ppm) to 13 V ([NO$_2$] = 15 ppm) to >20 V ([NO$_2$] = 30 ppm). At [NO$_2$] = 30 ppm the transfer curve becomes almost linear without a distinct off state in the gate voltage (V_G) region of +20 to -40 V.

The corresponding TFT μ and V_T parameters for different t_{UVO} and [NO$_2$] values are summarized in **Table 2**. Untreated devices exhibit minimal μ (4.0×10^{-3} to 4.4×10^{-3} cm^2 V^{-1} s^{-1}) and V_T (-14.8 to -13.3 V) changes upon NO$_2$ exposure. However, as the t_{UVO} increases, μ increases with increasing [NO$_2$], along with a large positive V_T shift. For example, μ for the transistor with a $t_{UVO} = 120$ s monotonously increases from 1.8×10^{-3} cm^2 V^{-1} s^{-1} ([NO$_2$] = 0 ppm) to 2.4×10^{-3} cm^2 V^{-1} s^{-1} ([NO$_2$] = 30 ppm) and the V_T shifts from -7.2 V ([NO$_2$] = 0 ppm) to +17 V ([NO$_2$] = 30 ppm). Furthermore, for the OTFT with a $t_{UVO} = 300$ s, μ increases from 8.3×10^{-4} cm^2 V^{-1} s^{-1} ([NO$_2$] = 0 ppm) to 1.5×10^{-3} cm^2 V^{-1} s^{-1} ([NO$_2$] = 30 ppm)

**ADVANCED
SCIENCE NEWS**
www.advancedsciencenews.com

**ADVANCED
MATERIALS**
www.advmat.de

Table 2. Summary of mobility and threshold voltage variations for different t_{UVO}-treated devices as a function of NO_2 concentration.

NO$_2$ con. [ppm]		t_{UVO} [s]							
		0	30	60	120	180	240	300	360
0	μ (10^{-3} cm^2 V^{-1} s^{-1})	4.0	3.5	2.8	1.8	1.6	1.4	0.8	0.8
5		4.0	3.5	2.7	1.9	1.6	1.5	0.9	0.9
10		4.1	3.6	2.9	2.0	1.7	1.7	1.1	1.1
15		4.2	3.6	3.0	2.0	1.8	1.8	1.2	1.2
20		4.2	3.6	3.0	2.1	1.9	1.9	1.4	1.4
25		4.3	3.7	3.1	2.3	2.1	2.0	1.5	1.5
30		4.4	3.8	3.3	2.4	2.1	2.1	1.5	1.5
0	V_T [V]	−14.8	−12.7	−8.8	−7.2	−7.0	−7.6	−7.5	−7.1
5		−14.7	−12.7	−7.7	−6.1	−5.9	−3.5	−2.6	−2.1
10		−14.4	−12.1	−4.0	−2.5	−2.1	2.2	3.0	3.6
15		−14.2	−11.3	−1.4	1.1	2.5	7.2	8.5	12.4
20		−13.9	−10.1	3.1	6.6	9.3	17.1	17.2	21.9
25		−13.6	−9.0	5.6	13.7	18.2	25.5	29.3	34.9
30		−13.3	−7.8	9.8	17.0	28.2	39.3	43.9	52.3

while V_T shifts from −7.5 V ([NO$_2$] = 0 ppm) to +43.9 V ([NO$_2$] = 30 ppm). The relative variations of both μ and V_T are summarized in Figure 1d, which also indicates that the TFT parameter shifts tend to saturate when $t_{UVO} \geq 300$ s, in agreement with the I–V characteristics.

An important sensor performance parameter is the sensitivity (S) to the given analyte. As is standard for TFT sensors,[22,28,29] the sensitivity (S) here for gas analyte is given by using Equation (1), where I_{Gas} is the drain current of the transistor

$$S = \left(\frac{I_{Gas} - I_0}{I_0} \right) \times 100\% \tag{1}$$

when exposed to gas analyte and I_0 is the drain current of the unexposed transistor. As shown in Figure 1e and Figure S5 (Supporting Information), the sensitivity to NO$_2$ increases as t_{UVO} increases, and since the transfer curve is V_G dependent, the sensitivity also depends on V_G with the highest sensitivity lying in the −15 to 0 V V_G region. Upon NO$_2$ exposure, the transfer curve shifts toward the upper-left corner of the transfer plot (Figure S4, Supporting Information), along with an enlarged I_{OFF}. Clearly, the highest sensitivity will not be in the region where the transistors are in the on-state, but close to the region where the original turn-on voltages are.

As shown in Figure 1e and Figure S5 (Supporting Information), for V_G = −40 V, the sensitivity at [NO$_2$] = 30 ppm is the largest and increases from ≈400% (t_{UVO} = 0 s) to ≈35 000% (t_{UVO} = 120 s) to ≈90 000% (t_{UVO} = 240 s), and saturates at t_{UVO} = ≈300 s with a sensitivity as high as ≈160 000%. Even for a low [NO$_2$] of 5 ppm, high sensitivity of ≈500% is achieved for the device with t_{UVO} = 360 s. In contrast, although the sensitivity at $V_D = V_G$ = −40 V is relatively low, ≈1600% for [NO$_2$] = 30 ppm, it is equally important since the saturation region usually has a much higher signal-to-noise ratio, the reliability of the data is enhanced. From Figure S5 (Supporting Information), the

sensitivity in saturation ($V_D = V_G$ = −40 V) for a [NO$_2$] = 30 ppm increases from ≈15% (t_{UVO} = 0 s) to ≈300% (t_{UVO} = 120 s) to ≈1000% (t_{UVO} = 240 s), and reaches maximum of ≈1600% at t_{UVO} = 360 s.

To illuminate the origin of the increased detection performance, the film morphologies of the gate dielectric (on top of ITO) and of the organic semiconductor (on top of the dielectric) were first probed by atomic force microscopy (AFM). Such film morphologies are known to affect the sensing performance of OTFT-based gas sensors.[40,41] AFM images of the dielectric films with various t_{UVO} treatments indicate negligible topological variations (**Figure 2**a and Figure S6, Supporting Information), with all films remaining very smooth with an RMS roughness of 0.24–0.29 nm. More interestingly, the CuPc films grown on the dielectric treated for different t_{UVO}'s also exhibit similar morphologies, which are characterized by small grains with ≈25 nm dimensions and a considerable density of grain boundaries (Figure 2b). The phase images of these films (see Figure 2c) further confirm that the semiconductor grain topology/mechanical properties and density remain unchanged with various t_{UVO}'s. A large density of grain boundaries will facilitate analyte diffusion to the dielectric/semiconductor interface, which can enhance the sensing performance of OTFTs.[42] However, since the quality of the grain boundaries does not change with t_{UVO}, these data demonstrate that this semiconductor morphology simply creates the condition for large sensitivity but it cannot underlie the detection mechanism in the present sensors. Moreover, grazing incidence X-ray diffraction (GIXRD) measurements (Figure 2d) indicate that all CuPc films exhibit the same strong (200) diffraction at 2θ = 6.9°.[43] By fitting the diffraction peaks to a Gaussian function, a full width at the half maximum (FWHM) of 0.55° ± 0.1° is obtained for all the (200) diffraction peaks, indicating that UVO treatment does not significantly affect CuPc crystallite dimensions (≈14.5 nm) or orientation on the dielectric film. Thus, semiconductor and dielectric film morphologies are

**ADVANCED
SCIENCE NEWS**

www.advancedsciencenews.com
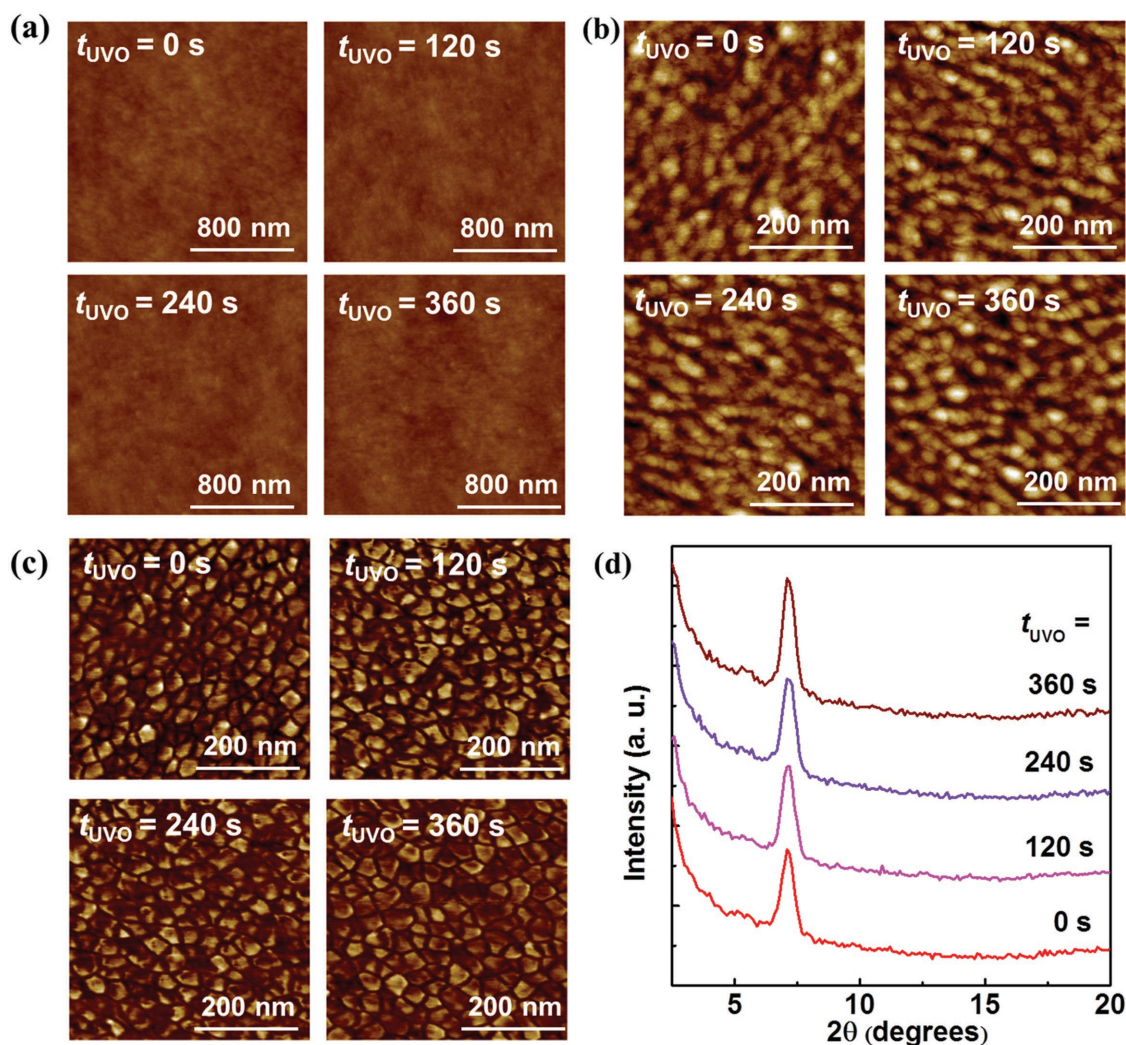
**ADVANCED
MATERIALS**

www.advmat.de

Figure 2. AFM images for the indicated t_{UVO} values of a) the PVA/PS gate dielectric films; b) CuPc (height image) and c) corresponding phase image films; d) GIXRD spectra of CuPc films grown on the PVA/PS gate dielectric as a function of t_{UVO}.

irrelevant to the enhanced sensitivities, which must therefore be chemical in nature.

X-ray photoelectron spectroscopy (XPS) was next utilized to analyze the surface chemical changes of the dielectric upon UVO treatment. As shown in **Figure 3**a and Figure S7 (Supporting Information), UVO introduces large densities of oxygen-containing species on the PS surface. In pristine PS/PVA films, there is no oxygen on the surface and carbon 1s peak fits well with only C−C/C−H components at 285.0 ± 0.1 eV and a C=C π–π* satellites at ≈292.5 eV. After UVO treatment, features corresponding to C−O, C=O, and O−C=O at 286.5 ± 0.1, 288.0 ± 0.1, and 289.5 ± 0.1 eV, respectively, can be identified.[44,45] Moreover, the density of the newly generated functional groups can be controlled by adjusting t_{UVO}, as shown in Table S2 (Supporting Information). To monitor the stability of the surface functional groups, the t_{UVO} = 360 s dielectric sample was aged in air for one month, and then analyzed by XPS. As shown in Figure S8 (Supporting Information), similar carbon content is obtained for the pristine and aged PS surfaces, with only a slightly decrease in C content (from 65.1% to 64.5%)

and a small increase of O content (from 34.9% to 35.5%), indicating that UVO-generated functional groups on the surface are stable in air. The existence of new carbon-oxygen groups was also confirmed by Fourier transform infrared spectroscopy (FT-IR) on pristine and UVO-treated PS/PVA films. In Figure 3b and Figure S9 (Supporting Information), the vibrational peaks at ≈1452, ≈1492, and ≈1600 cm^{-1}, and multipeaks in the 2800–3110 cm^{-1} range from all dielectric films indicate the existence of the principle chemical bonds (C−C and C−H) revealing that UVO treatment only changes the surface chemical environment of the top PS film.[46–48] However, a new peak at ≈1728 cm^{-1} intensifies as the t_{UVO} increases, indicating the generation of C=O and/or O−C=O groups.[49] Moreover, the weak broad band at ≈3500 cm^{-1} for treated films implies that hydroxyl groups are produced, possibly originating from C−OH, and COOH functional groups as well as physisorbed water molecules.

PS is known to be an excellent gate dielectric material for both n-type and p-type organic semiconductor TFTs.[50] However, PS surface treatment with UVO is known to affect OSC
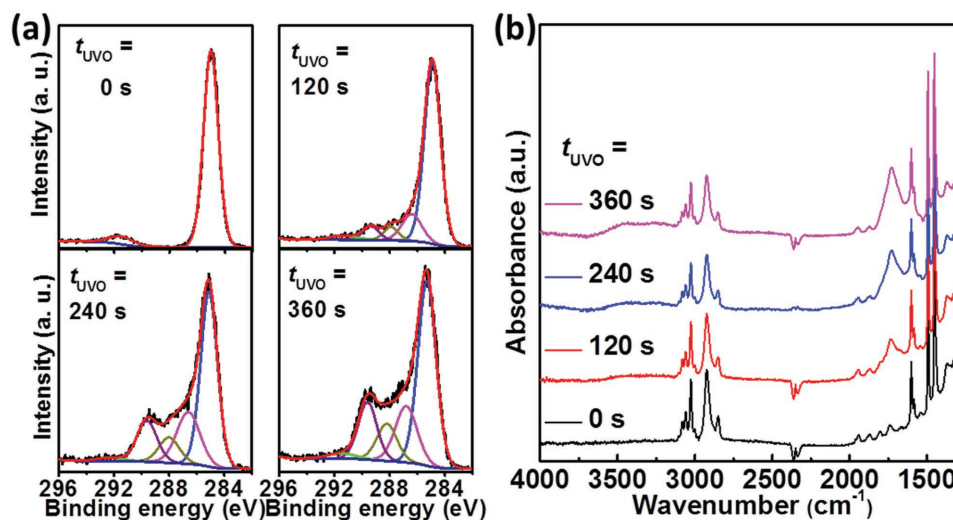
**ADVANCED
SCIENCE NEWS**
www.advancedsciencenews.com

**ADVANCED
MATERIALS**
www.advmat.de

Figure 3. a) C 1s XPS and b) FT-IR of PVA/PS dielectric films as a function of t_{UVO}.

transport characteristics.[51] For the present PVA/PS-CuPc devices, the slightly reduced I_{ON} ($\approx 1.6 \times 10^{-6} \to \approx 3.2 \times 10^{-7}$ A) and μ ($\approx 3 \times 10^{-3} \to \approx 5 \times 10^{-4}$ cm^2 V^{-1} s^{-1}) upon UVO treatment ($t_{UVO} = 0 \to 360$ s) reveal that shallow traps are created by the UVO processing (Figure S1, Supporting Information, and Table 1). Furthermore, a slight shift of V_T in the positive direction is observed, however considering the nonlinearity of $(I_{ON})^{1/2}$ versus V_G, an accurate estimation of the trap density variation from V_T variation is not possible. When the devices are exposed to the analyte, the NO_2 molecules freely diffuse through the semiconductor grain boundaries and reach the PS/CuPc interface.[52–54] As described previously, these devices exhibit significant changes in I–V characteristics, with substantial increases of both I_{ON} and μ as well as a dramatic negative shift of V_T to positive values. The shifts in all of these parameters increase as [NO_2] increases (Table 2). Furthermore, plots of $(I_{ON})^{1/2}$ versus V_G show excellent linearity (**Figure 4**a and Figure S10, Supporting Information), enabling calculation of the trap density variation from ΔV_T utilizing the equation

$$\Delta N_{tr} = \frac{C_i \Delta V_T}{e}.[55]$$ Note, close inspection of the I–V characteristics points to a positively shifted V_T and an enlarged subthreshold slope (SS), which is due to a simultaneous detrapping and doping processes. This result is in agreement with charge transport studies on doped CuPc based OTFT.[56] Here, the approximate energy of the donor states, deduced from the TFT characteristics, results from a shallow and narrow doping state shifting the V_T but not affecting SS, and a second doping state which is distributed from the band edge to a binding energy of about 0.3 eV, leading to a broadened subthreshold region.[57] Thus, SS variation will not only be dominated by the detrapping process, which would decrease SS. However, both detrapping and/or hole doping processes will always shift V_T to the positive direction, thus it can be utilized to simulate the overall trap state variations.[56] Details of the state density variations are summarized in Table S3 (Supporting Information) and Figure 4b. As an example, the state density of the devices with $t_{UVO} = 0$ s varies by $\approx 15.3 \times 10^{10}$ cm^{-2} on going from the unexposed to the 30 ppm NO_2 exposed device, while those with

$t_{UVO} = 360$ s exhibit a substantial density variations of 689.0×10^{10} cm^{-2} over the same analyte concentration range. Clearly, the higher the [NO_2], the more mobile holes are generated in the semiconductor channel.

A key question is how combined UVO surface activation and NO_2 chemistry enable the present sensing mechanism. As discussed above, the pristine PVA/PS dielectric has a low polarity surface covered with carbon–hydrogen bonds and should have negligible binding affinity for NO_2 molecules. As shown in Figure 1c and Figure S4 (Supporting Information), the devices without UVO treatment of the dielectric layer exhibit minimal changes in the I–V characteristics on NO_2 exposures as high as 30 ppm. This result indicates that although NO_2 is a strong oxidizing agent[58] and can efficiently penetrate the organic semiconductor, it is apparently unable to chemically oxidize (p-dope) the bulk of CuPc and when no NO_2 adsorption on the dielectric surface occurs, since this process alone would greatly enhance CuPc bulk conductivity and therefore I_{OFF} of all of the present OTFTs, including those without or with brief dielectric UVO exposure. On the other hand, upon UVO treatment, large densities of oxygenated polar functionalities are produced on the dielectric surface (Figure 3), which should efficiently adsorb polar molecules such as NO_2 via hydrogen bonding or van der Waals interactions.[59] Polarization effects would then induce positive charges in the semiconductors (Figure 4c). Furthermore, the polar UVO exposed surfaces may also have significant quantities of adsorbed water molecules, which would react with NO_2 + O_2 to produce nitric acid.[60] Highly acidic, strongly adsorbed HNO_3 can protonate/dope the first semiconductor monolayer yet is volatile enough to evaporate under low pressures to recover sensor function (vide infra).

To demonstrate the interfacial origin of sensing mechanism and corroborate that it is due to the UVO of the PS surface, we carried FT-IR experiments. Initial experiments, performed on the exact CuPc(semiconductor)/PS/PVA(dielectric) layers used in the TFT measurements (Figure S11, Supporting Information), were inconclusive since the IR peaks of the thick dielectric (C−C and C−H PS stretching modes)[61] overlap and are stronger than that possibly ascribable to NO_2 (≈ 1600 cm^{-1}).[62]

ADVANCED
SCIENCE NEWS

www.advancedsciencenews.com

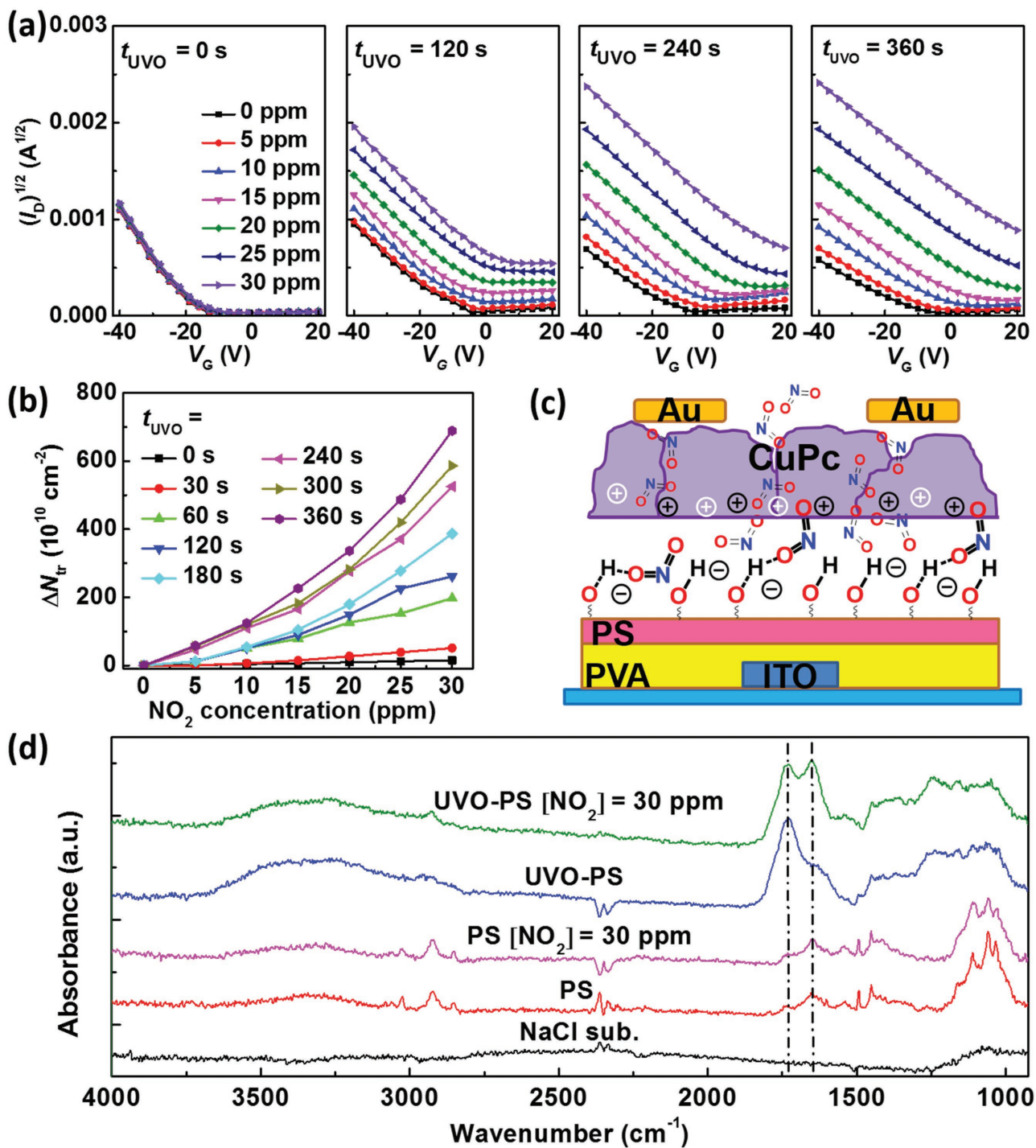**ADVANCED
MATERIALS**

www.advmat.de

Figure 4. a) Square root of drain current versus gate voltage plots for different t_{UVO} values at the indicated NO_2 concentrations. b) Trap density as a function of NO_2 concentration for different t_{UVO}. c) Schematic representations of the NO_2 diffusion process through the semiconductor grain boundaries and mobile positive charge carrier formation by NO_2 adsorption to the UVO-treated PS surface (black positive charges) and field-effect (white positive charges). d) FT-IR of the indicated samples with t_{UVO} = 0 or 360 s and $[NO_2]$ = 0 or 30 ppm (5 min).

However, these data support that no bulk penetration/adsorption of NO_2 into the dielectric nor chemical reactions with CuPc/PS/PVA occur. Thus, we utilized an alternative platform consisting of a thin PS film ($\approx$10 nm) on IR-transparent NaCl to minimize noise and retain the dielectric surface characteristics.

As shown in Figure 4d, PS on NaCl shows distinct vibrational peaks at $\approx$1452, $\approx$1492, $\approx$1600, and $\approx$2800–3110 cm^{-1}, in agreement with the literature.[48] After sample expose to 30 ppm NO_2 for 5 min, no newly generated peaks are detected. UVO-exposed PS samples (t_{UVO} = 360 s) reveal the formation of an intense

**ADVANCED
SCIENCE NEWS**
www.advancedsciencenews.com

**ADVANCED
MATERIALS**
www.advmat.de

peak at ≈1728 cm^{-1}, assigned to C=O functional groups,[49] as well as increased/broadening of the IR hydroxyl region (3000–3500 cm^{-1}). Importantly, the IR spectrum of the UVO-treated PS films exposed to 30 ppm NO_2 for 5 min exhibits a new strong peak at ≈1630 cm^{-1}, assignable to adsorbed NO_2. Note for PS films, the peak at ≈1650 cm^{-1} is expected for monosubstituted aromatic rings.[48] Thus, the combined IR experiments demonstrate that UVO generates new polar groups on the PS surface, NO_2 does not chemically react with the dielectric bulk/surface, and that our UVO-treated dielectric platform has the ability to physically adsorb NO_2.

Real-time sensitivities were next measured for devices biased at $V_D = V_G = -40$ V, responding to the dynamic switching to low NO_2 exposures (1, 2, 4, 6, 8, and 10 ppm, **Figure 5**a). The sensitivity at all the concentrations increases dramatically for devices with longer t_{UVO}'s. For example, the sensitivity at 6 ppm NO_2 increases from 10% ($t_{UVO} = 0$ s) to ≈700% ($t_{UVO} = 120$ s), ≈1800% ($t_{UVO} = 240$ s), and ≈3200% ($t_{UVO} = 360$ s). In fact, the sensitivity enhancement is so large that the response in devices without UVO-treated dielectric cannot be displayed (Figure 5a), and a separate plot with a much smaller Y-axis is required (inset of Figure 5a). Furthermore, for a low 1 ppm NO_2 concentration, the sensitivity for $t_{UVO} = 0$ s devices is only ≈4%, which can barely be integrated for practical applications. However, for devices with $t_{UVO} = 360$ s, the sensitivity for 1 ppm NO_2 increases to a remarkable ≈200%, which is distinguishable with any sample analyzer. Due to the limitation of

the test equipment, 1 ppm is the lowest concentration of NO_2 that can be reliably utilized in these experiments. However, the estimated LOD for this platform can be calculated using Equation (2),[33,63] where $\eta = 1.645$ corresponds to the 90% confidence

$$Y_{LOD} = \frac{-a \times b + \sqrt{a^2 \times b^2 - (b^2 - \eta^2 \times \Delta b^2)(a^2 - \eta^2 \times \Delta a^2)}}{b^2 - \eta^2 \times \Delta b^2} \quad (2)$$

level, a, b, Δa, and Δb are the parameters extracted from the linear fit of Figure S12 (Supporting Information), based on sensitivities of the device with $t_{UVO} = 120$ s. This yields a LOD of 415 ppb. These sensitivities are among the highest reported to date for NO_2 sensors based on either resistor (S as high as 900% for 20 ppm NO_2, and 300% for 5 ppm NO_2) or TFT (S as high as 120% for 30 ppm NO_2, and 80% for 5 ppm NO_2) architectures.[5,30,64–67] Note that earlier studies demonstrated LOD for NO_2 lower than ≈53 ppb, the concentration which is considered safe by the U.S. Environmental Control Agency.[68–70] However, our current sensor platform can detect concentrations much lower than those which are of concern for "long-term exposure" (≈1 ppm).[5] Thus, our very simple TFT structure with a sensitivity of ≈400 ppb is more than sufficient to immediately alert that the environment is becoming unsafe and precautions should be taken. Furthermore, even lower LODs could be possible by, for instance, optimizing the dielectric surface
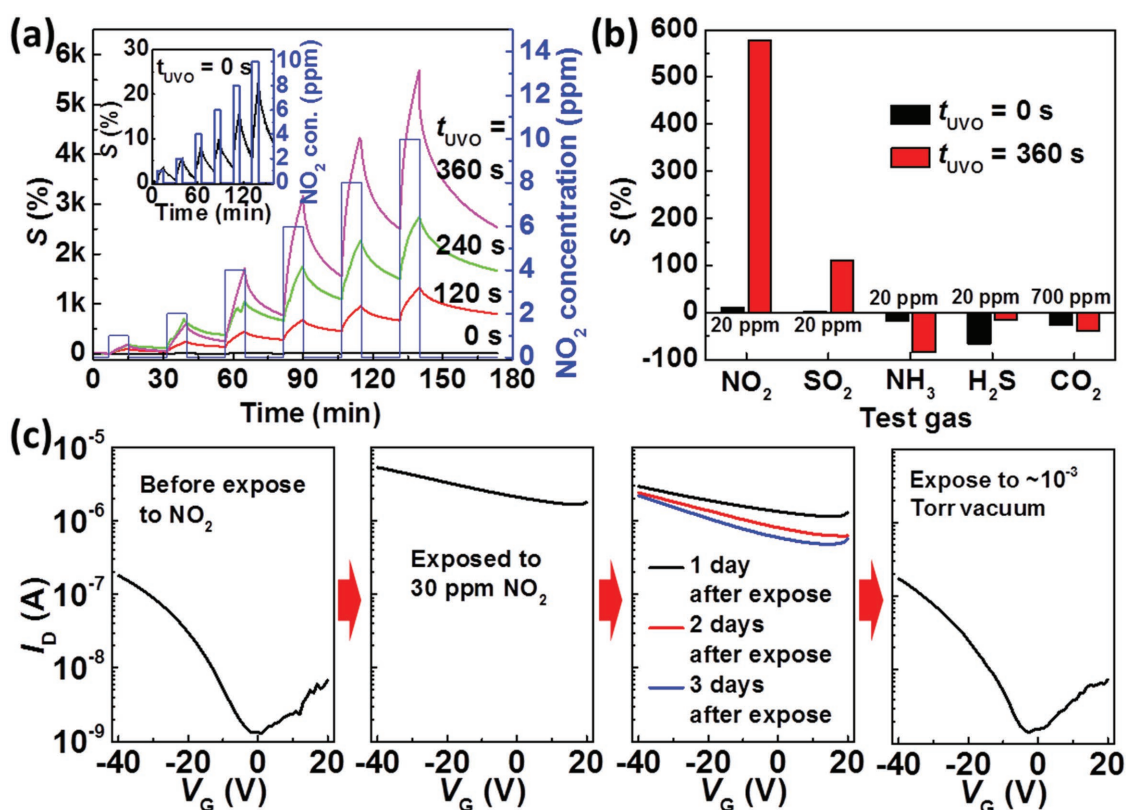

Figure 5. a) Real-time sensitivity ($V_D = V_G = -40$ V) responding to dynamic switching between NO_2 concentrations. b) Sensitivities of sensors with both $t_{UVO} = 0$ and 360 s for 20 ppm NO_2, SO_2, NH_3, H_2S, and 700 ppm CO_2. c) Transfer curves of a transistor with 360 s UVO-treated dielectric when tested under different environments.

**ADVANCED
SCIENCE NEWS**
www.advancedsciencenews.com

**ADVANCED
MATERIALS**
www.advmat.de

chemistry using other polymers, vary the TFT channel lengths, and the organic semiconductor type/film morphology,[42] all approaches that will not enhances device complexity or costs.

For practical applications, selectivity is another important parameter, which was tested for the devices with both $t_{UVO} = 0$ and 360 s at concentrations of 20 ppm for NO_2, SO_2, NH_3, and H_2S and at a concentration of 700 ppm for CO_2 (since dry air is utilized as the carrier gas which itself contains ≈400 ppm CO_2, thus more CO_2 is mixed into dry air to have a higher concentration of CO_2). As shown in Figure 5b. it is clear that for the optimized platform ($t_{UVO} = 360$ s) all of the other gases are at least 6× less sensitive than NO_2. Thus, for NO_2 the sensitivity increased from 10% ($t_{UVO} = 0$ s) to almost 600% ($t_{UVO} = 360$ s) at a concentration of 20 ppm whereas for SO_2 (the most sensitive of the other gases) sensitivity increased from 3% ($t_{UVO} = 0$ s) to 110% ($t_{UVO} = 360$ s) for the same concentration. The TFT sensitivity for the other gases at the same concentration is far less and, equally important, the current variation is opposite compared to those of NO_2 and SO_2. Thus, the sensitivity for NH_3 increased from −17% ($t_{UVO} = 0$ s) to −84% ($t_{UVO} = 360$ s), while for H_2S, the sensitivity decreased from −66% ($t_{UVO} = 0$ s) to −16% ($t_{UVO} = 360$ s). For the apolar CO_2, even at the high concentration of 700 ppm, the sensor with/without UVO treatment both revealed a relatively low sensitivity of <38%. From Figure 5b, it can be concluded that our sensors are extremely sensitive to NO_2 compared to other four kinds of common gas pollutants. Moreover, this platform can distinguish between strongly oxidizing/polar (NO_2, SO_2) versus reducing/polar gases (NH_3 and H_2S) and weekly acidic/apolar (CO_2) one. These differences could be further optimized by properly optimizing t_{UVO}, fabricating platforms with TFT arrays with dielectric surfaces with different t_{UVO} (currently under investigation), and using other semiconducting materials.

Finally, note that after TFT exposure to NO_2, the recovery times of the I–V characteristics for the UVO-treated devices are relatively long. As shown in Figure 5c, when the UVO-treated TFT ($t_{UVO} = 360$ s) is exposed to 30 ppm NO_2 for 5 min, the subsequent transfer curve remains flat, not recovering the original shape after storage in air for 3 d. However, by placing the NO_2 exposed device in ≈10^{-3} Torr vacuum, the transfer curve quickly recovers to its original shape (Figure 5c), corroborating that NO_2 is likely physisorbed on the dielectric/semiconductor interface rather than irreversibly reacting. Moreover, when the device characteristics are recovered in vacuum, they can be reused (Figure S13, Supporting Information). Although the recovery of the UVO-treated transistors is not fast and complete (Figure 5c), it is possible to accelerate recovery by increasing the working temperature, typical of other OTFT gas sensors.[68] That physisorption is stable under the present conditions indicates that the current platform can be utilized as an integrator to record maximum NO_2 exposure.[24] Coupled with a proper alarm, such a device could be used to signal when dangerous NO_2 levels are reached.

In summary, OTFT-based NO_2 sensors with ultrahigh sensitivities and good selectivities have been realized via UVO treatment of the gate dielectric surface. UVO generates oxygen-containing functional groups capable of strongly interacting with NO_2, which underlies the sensing mechanism. The NO_2 device sensitivity approaches ≈200% and ≈160 000% for NO_2

concentrations of 1 and 30 ppm, respectively. This simple processing addresses the low sensitivity and high LOD of conventional gas sensors based on OTFTs. Thus, we believe that the present strategy, together with the advantages of simple OTFT fabrication, opens new opportunities to realize high-performance, low-cost, portable electronic noses.

Experimental Section

Transistor Fabrication: PVA (M_w = 146 000–186 000, 99+% hydrolyzed, Sigma-Aldrich) was dissolved in DI water with a concentration of 4 wt%. PS (average M_w ≈ 280 000, Sigma-Aldrich) was dissolved in xylene with a concentration of 3 wt%. Indium tin oxide[48] glass substrate was cleaned sequentially in an ultrasonic bath with acetone, deionized water, and isopropyl alcohol for 15 min each. PVA was then spin-coated at 3000 rpm for 1 min, and annealed at 70 °C for 1 h on a hot plate. PS was then spin-coated at 3000 rpm for 1 min. After dielectric layer coating, the substrates were baked at 120 °C for 1 h to completely remove residual solvents. Prior to the deposition of organic semiconductors, the dielectrics were exposed to UV light of 185 and 253.7 nm (UVO-Cleaner 42, Jelight Company Inc.) for 0–360 s. 10 nm CuPc was then evaporated under 4×10^{-6} Torr at a rate of 0.2–0.3 Å s^{-1}. The transistors were completed by depositing the source and drain electrodes of 40 nm gold via thermal evaporation using a metal shadow mask under 4×10^{-6} Torr at a rate of 0.5–1 Å s^{-1}.

Device Characterization and Sensor Evaluation: TFT characterization was performed in air on a custom probe station using an Agilent 1500 semiconductor parameter analyzer. The electron mobility (μ) was calculated in the saturation region using Equation (3)

$$I_D = \frac{WC_i}{2L} \mu (V_G - V_T)^2 \tag{3}$$

where C_i is the capacitance per unit area of dielectric layer, and W and L are channel width and length, respectively. For sensing tests, the OTFT sensor was stored in an airtight test chamber (≈2.4 mL). A mixture of dry air and certain gas analyte (50 ppm standard NO_2 gas, 50 ppm standard SO_2 gas, 50 ppm standard NH_3 gas, 50 ppm standard H_2S gas, or 1000 ppm standard CO_2 gas) in appropriate concentrations was introduced into the test chamber by mass flow controllers. The flow rate in the test was fixed at 100 sccm (standard cm^3 min^{-1}).

Film Characterization: AFM film topographies were imaged with a Veeco Dimension Icon scanning Probe Microscope using tapping mode. GIXRD measurements were carried out on a Rigaku SmartLab workstation (CuKα, λ = 1.542 Å) with an incident angle (α = 0.5°). XPS was performed on Thermo Scientific ESCALAB 250Xi at a base pressure of 4.5×10^{-10} mbar (UHV). FT-IR spectra were collected by Nexus 870 spectrometer (Thermo Nicolet) with a single reflection horizontal ATR accessory having a diamond ATR crystal fixed at incident angle of 45°.

Supporting Information

Supporting Information is available from the Wiley Online Library or from the author.

Acknowledgements

**ADVANCED
SCIENCE NEWS**

www.advancedsciencenews.com

**ADVANCED
MATERIALS**

www.advmat.de

Conflict of Interest

The authors declare no conflict of interest.

Keywords

[1] P. Nejat, F. Jomehzadeh, M. M. Taheri, M. Gohari, M. Z. Abd Majid, *Renewable Sustainable Energy Rev.* **2015**, *43*, 843.

[2] Y. X. He, Y. Xu, Y. X. Pang, H. Y. Tian, R. Wu, *Renewable Energy* **2016**, *89*, 695.

[3] Y. Guo, G. Yu, Y. Liu, *Adv. Mater.* **2010**, *22*, 4427.

[4] G. B. Hamra, F. Laden, A. J. Cohen, O. Raaschou-Nielsen, M. Brauer, D. Loomis, *Environ. Health Perspect.* **2015**, *123*, 1107.

[5] A. Das, R. Dost, T. Richardson, M. Grell, J. J. Morrison, M. L. Turner, *Adv. Mater.* **2007**, *19*, 4018.

[6] T. W. Hesterberg, W. B. Bunn, R. O. McClellan, A. K. Hamade, C. M. Long, P. A. Valberg, *Crit. Rev. Toxicol.* **2009**, *39*, 743.

[7] R. Pohanish, *Sittig's Handbook of Toxic and Hazardous Chemicals and Carcinogens*, 6th ed., William Andrew, New York, **2011**.

[8] A.-M. Andringa, C. Piliego, I. Katsouras, P. W. M. Blom, D. M. d. Leeuw, *Chem. Mater.* **2014**, *26*, 773.

[9] Y. Zang, D. Huang, C. A. Di, D. Zhu, *Adv. Mater.* **2016**, *28*, 4549.

[10] A. Luzio, F. G. Ferré, F. D. Fonzo, M. Caironi, *Adv. Funct. Mater.* **2014**, *24*, 1790.

[11] K.-J. Baeg, M. Caironi, Y.-Y. Noh, *Adv. Mater.* **2013**, *25*, 4210.

[12] M. J. Sung, A. Luzio, W.-T. Park, R. Kim, E. Gann, F. Maddalena, G. Pace, Y. Xu, D. Natali, C. de Falco, L. Dang, C. R. McNeill, M. Caironi, Y.-Y. Noh, Y.-H. Kim, *Adv. Funct. Mater.* **2016**, *26*, 4984.

[13] C. Zhang, P. Chen, W. Hu, *Chem. Soc. Rev.* **2015**, *44*, 2087.

[14] S. J. Han, W. Huang, W. Shi, J. S. Yu, *Sens. Actuators, B* **2014**, *203*, 9.

[15] S. J. Han, X. M. Zhuang, W. Shi, X. Yang, L. Li, J. S. Yu, *Sens. Actuators, B* **2016**, *225*, 10.

[16] K. H. Cheon, J. Cho, Y. H. Kim, D. S. Chung, *ACS Appl. Mater. Interfaces* **2015**, *7*, 14004.

[17] M. Magliulo, A. Mallardi, R. Gristina, F. Ridi, L. Sabbatini, N. Cioffi, G. Palazzo, L. Torsi, *Anal. Chem.* **2013**, *85*, 3849.

[18] W. G. Huang, J. Sinha, M. L. Yeh, J. F. M. Hardigree, R. LeCover, K. Besar, A. M. Rule, P. N. Breysse, H. E. Katz, *Adv. Funct. Mater.* **2013**, *23*, 4094.

[19] W. Shi, X. E. Yu, Y. F. Zheng, J. S. Yu, *Sens. Actuators, B* **2016**, *222*, 1003.

[20] H. Zhang, X. Guo, J. Hui, S. Hu, W. Xu, D. Zhu, *Nano Lett.* **2011**, *11*, 4939.

[21] M. Magliulo, K. Manoli, E. Macchia, G. Palazzo, L. Torsi, *Adv. Mater.* **2015**, *27*, 7528.

[22] T. Shaymurat, Q. Tang, Y. Tong, L. Dong, Y. Liu, *Adv. Mater.* **2013**, *25*, 2269.

[23] Y. Zang, F. Zhang, D. Huang, C. A. Di, Q. Meng, X. Gao, D. Zhu, *Adv. Mater.* **2014**, *26*, 2862.

[24] W. G. Huang, K. Besar, R. LeCover, A. M. Rule, P. N. Breysse, H. E. Katz, *J. Am. Chem. Soc.* **2012**, *134*, 14650.

[25] W. G. Huang, K. Besar, R. LeCover, P. Dulloor, J. Sinha, J. F. M. Hardigree, C. Pick, J. Swavola, A. D. Everett, J. Frechette, M. Bevan, H. E. Katz, *Chem. Sci.* **2014**, *5*, 416.

[26] F. X. Werkmeister, T. Koide, B. A. Nickel, *J. Mater. Chem. B* **2016**, *4*, 162.

[27] K. C. See, A. Becknell, J. Miragliotta, H. E. Katz, *Adv. Mater.* **2007**, *19*, 3322.

[28] M. Mirza, J. Wang, D. Li, S. A. Arabi, C. Jiang, *ACS Appl. Mater. Interfaces* **2014**, *6*, 5679.

[29] L. Li, P. Gao, M. Baumgarten, K. Mullen, N. Lu, H. Fuchs, L. Chi, *Adv. Mater.* **2013**, *25*, 3419.

[30] H. D. Fan, W. Shi, X. G. Yu, J. S. Yu, *Synth. Met.* **2016**, *211*, 161.

[31] M. W. G. Hoffmann, J. D. Prades, L. Mayrhofer, F. Hernandez-Ramirez, T. T. Järvi, M. Moseler, A. Waag, H. Shen, *Adv. Funct. Mater.* **2014**, *24*, 595.

[32] D. Khim, G. S. Ryu, W. T. Park, H. Kim, M. Lee, Y. Y. Noh, *Adv. Mater.* **2016**, *28*, 2752.

[33] M. Mirza, J. W. Wang, L. Wang, J. He, C. Jiang, *Org. Electron.* **2015**, *24*, 96.

[34] A. Klug, M. Denk, T. Bauer, M. Sandholzer, U. Scherf, C. Slugovc, E. J. W. List, *Org. Electron.* **2013**, *14*, 500.

[35] J. Zhang, X. Liu, G. Neri, N. Pinna, *Adv. Mater.* **2016**, *28*, 795.

[36] J. R. Vig, *J. Vac, Sci. Technol., A* **1985**, *3*, 1027.

[37] W. Huang, X. G. Yu, H. D. Fan, J. S. Yu, *Appl. Phys. Lett.* **2014**, *105*, 093302.

[38] S. J. Han, J. H. Kim, J. W. Kim, C. K. Min, S. H. Hong, D. H. Kim, K. H. Baek, G. H. Kim, L. M. Do, Y. Park, *J. Appl. Phys.* **2008**, *104*, 013715.

[39] A. Wang, I. Kymissis, V. Bulovic, A. I. Akinwande, *Appl. Phys. Lett.* **2006**, *89*, 112109.

[40] Y. S. Rim, S. H. Bae, H. Chen, N. De Marco, Y. Yang, *Adv. Mater.* **2016**, *28*, 4415.

[41] W. Huang, J. S. Yu, X. G. Yu, W. Shi, *Org. Electron.* **2013**, *14*, 3453.

[42] D. Duarte, A. Dodabalapur, *J. Appl. Phys.* **2012**, *111*, 044509.

[43] A. C. Cruickshank, C. J. Dotzler, S. Din, S. Heutz, M. F. Toney, M. P. Ryan, *J. Am. Chem. Soc.* **2012**, *134*, 14302.

[44] D. O. H. Teare, C. Ton-That, R. H. Bradley, *Surf. Interface Anal.* **2000**, *29*, 276.

[45] M. M. Browne, G. V. Lubarsky, M. R. Davidson, R. H. Bradley, *Surf. Sci.* **2004**, *553*, 155.

[46] Y. Konuklu, M. Ostry, H. O. Paksoy, P. Charvat, *Energy Build.* **2015**, *106*, 134.

[47] E. Biazar, R. Zeinali, N. Montazeri, K. Pourshamsian, M. J. Behrouz, A. Asefnejad, A. Khoshzaban, G. Shahhosseini, M. S. Najafabadi, R. Abyani, H. Jamalzadeh, M. Fouladi, S. R. Hagh, A. S. Khamaneh, S. Kabiri, S. H. Keshel, A. Mansourkiaei, *Int. J. Nanomed.* **2010**, *5*, 549.

[48] D. Olmos, E. V. Martin, J. Gonzalez-Benito, *Phys. Chem. Chem. Phys.* **2014**, *16*, 24339.

[49] A. N. Yusilawati, M. Maizirwan, I. Sopyan, M. S. Hamzah, K. H. Ng, C. S. Wong, *Adv. Mater. Res.* **2011**, *264*, 1532.

[50] M. H. Yoon, C. Kim, A. Facchetti, T. J. Marks, *J. Am. Chem. Soc.* **2006**, *128*, 12851.

[51] N. V. Subbarao, M. Gedda, P. K. Iyer, D. K. Goswami, *ACS Appl. Mater. Interfaces* **2015**, *7*, 1915.

[52] X. Li, Y. D. Jiang, G. Z. Xie, H. L. Tai, P. Sun, B. Zhang, *Sens. Actuators, B* **2013**, *176*, 1191.

[53] J. H. Park, J. E. Royer, E. Chagarov, T. Kaufman-Osborn, M. Edmonds, T. Kent, S. Lee, W. C. Trogler, A. C. Kummel, *J. Am. Chem. Soc.* **2013**, *135*, 14600.

[54] J. H. Park, S. Lee, A. C. Kummel, *J. Vac. Sci. Technol., B* **2015**, *33*, 030604.

[55] V. Podzorov, E. Menard, A. Borissov, V. Kiryukhin, J. A. Rogers, M. E. Gershenson, *Phys. Rev. Lett.* **2004**, *93*, 086602.

[56] J. Park, J. E. Royer, C. N. Colesniuc, F. I. Bohrer, A. Sharoni, S. Jin, I. K. Schuller, W. C. Trogler, A. C. Kummel, *J. Appl. Phys.* **2009**, *106*, 034505.

[57] R. A. Street, M. L. Chabinyc, F. Endicott, *Phys. Rev. B* **2007**, *76*, 045208.

[58] A. M. Andringa, W. S. C. Roelofs, M. Sommer, M. Thelakkat, M. Kemerink, D. M. de Leeuw, *Appl. Phys. Lett.* **2012**, *101*, 153302.

[59] J. Y. Dai, J. M. Yuan, *Chem. Phys.* **2012**, *405*, 161.

[60] G. Murdachaew, M. E. Varner, L. F. Phillips, B. J. Finlayson-Pitts, R. B. Gerber, *Phys. Chem. Chem. Phys.* **2013**, *15*, 204.

[61] L. Harris, G. W. King, *J. Chem. Phys.* **1934**, *2*, 51.

[62] E. Flores, J. Viallon, P. Moussay, F. Idrees, R. I. Wielgosz, *Anal. Chem.* **2012**, *84*, 10283.

[63] H. Zheng, B. Ramalingam, V. Korampally, S. Gangopadhyay, *Appl. Phys. Lett.* **2013**, *103*, 193305.

[64] W. Yuan, L. Huang, Q. Zhou, G. Shi, *ACS Appl. Mater. Interfaces* **2014**, *6*, 17003.

[65] C. J. Qiu, Y. W. Dou, Q. L. Zhao, W. Qu, J. Yuan, Y. M. Sun, M. S. Cao, *Chin. Phys. Lett.* **2008**, *25*, 3590.

[66] N. Iqbal, A. Afzal, N. Cioffi, L. Sabbatini, L. Torsi, *Sens. Actuators, B* **2013**, *181*, 9.

[67] S. Ji, H. Wang, T. Wang, D. Yan, *Adv. Mater.* **2013**, *25*, 1755.

[68] A. M. Andringa, N. Vlietstra, E. C. P. Smits, M. J. Spijkman, H. L. Gomes, J. H. Klootwijk, P. W. M. Blom, D. M. de Leeuw, *Sens. Actuators, B* **2012**, *171*, 1172.

[69] A. Oprea, U. Weimar, E. Simon, M. Fleischer, H. P. Frerichs, C. Wilbertz, M. Lehmann, *Sens. Actuators, B* **2006**, *118*, 249.

[70] J. Li, Y. J. Lu, Q. Ye, M. Cinke, J. Han, M. Meyyappan, *Nano Lett.* **2003**, *3*, 929.

1701706 (11 of 11)